JOURNAL OF GEOPHYSICAL RESEARCH, VOL. 111, E12S13, doi:10.1029/2006JE002770, 2006

One Martian year of atmospheric observations using MER Mini-TES

Michael D. Smith,[1] Michael J. Wolff,[2] Nicole Spanovich,[3] Amitabha Ghosh,[4] Don Banfield,[5] Philip R. Christensen,[6] Geoffrey A. Landis,[7] and Steven W. Squyres[5]

Received 9 June 2006; revised 1 August 2006; accepted 16 August 2006; published 16 December 2006.

[1] The Spirit and Opportunity Mars Exploration Rovers (MER) landed on the surface of Mars in January 2004. Thermal infrared spectra taken by the Miniature Thermal Emission Spectrometer (Mini-TES) instrument on board each rover, collected in both the upward-looking and downward-looking geometries, has allowed for the retrieval of atmospheric temperatures between 1 and 2000 m above the surface, the column optical depth of dust, and the column abundance of water vapor for more than one full Martian year. During this period, Mini-TES has observed the annual cycle of temperature variations, the diurnal growth and decay of a near-surface highly superadiabatic layer, and random temperature fluctuations on a timescale of less than a minute. Mini-TES observations also record the timing, duration, and intensity of several local-scale and regional-scale dust storms and the annual variation of water vapor abundance at the two rover locations.

Citation: Smith, M. D., M. J. Wolff, N. Spanovich, A. Ghosh, D. Banfield, P. R. Christensen, G. A. Landis, and S. W. Squyres (2006), One Martian year of atmospheric observations using MER Mini-TES, *J. Geophys. Res.*, *111*, E12S13, doi:10.1029/2006JE002770.

1. Introduction

[2] Spectra returned by the Miniature Thermal Emission Spectrometer (Mini-TES) on board the Spirit and Opportunity Mars Exploration Rovers (MER) give the first view of the Martian surface and atmosphere in the thermal infrared from the surface of Mars [*Christensen et al.*, 2004a, 2004b]. Upward-looking observations by Mini-TES allow the temperature profile within the lowest 2 km of the planetary boundary layer (PBL) to be retrieved [*Smith et al.*, 2004]. The PBL is the portion of the atmosphere that directly interacts with the surface, responding to forcings such as frictional drag and surface heating. Mini-TES observations are important because they provide a glimpse of the convective and turbulent behavior of the temperature perturbations in the PBL, and these processes control the transfer of heat, momentum, and molecular species across the surface-atmosphere interface. Retrieved PBL temperature profiles also provide valuable constraints for the validation of boundary layer schemes used in both global and mesoscale Martian atmospheric models.

[3] A similar instrument, the Thermal Emission Spectrometer (TES), on board the Mars Global Surveyor [*Christensen et al.*, 2001] has been used extensively to retrieve the spatial and temporal variations of atmospheric temperatures and aerosol properties from orbit [e.g., *Conrath et al.*, 2000; *Wolff and Clancy*, 2003; *Smith*, 2004]. However, atmospheric temperatures retrieved from orbital observations such as TES do not have sufficient vertical resolution to resolve the PBL [*Conrath*, 1972; *Hinson et al.*, 2004].

[4] There have been relatively few direct measurements of meteorological parameters in the Martian PBL. The two Viking Landers directly measured temperature in the PBL during parachute descent [*Seiff and Kirk*, 1977], and after landing Viking and the Pathfinder lander measured temperature, pressure, and wind velocity, but at only a few selected heights within 1.5 m of the surface [*Hess et al.*, 1977; *Sutton et al.*, 1978; *Schofield et al.*, 1997]. Radio occultation experiments by Mariner 9 [*Kliore et al.*, 1973], the Viking Orbiters [*Lindal et al.*, 1979], and the Mars Global Surveyor [*Hinson et al.*, 1999, 2004] provide temperature profiles within the PBL but only at scattered locations and local times. Therefore the atmospheric temperatures retrieved from Mini-TES provide important new information about temperatures in the PBL that are complementary to many previous observations.

[5] In this paper we present the results of atmospheric retrievals from Mini-TES spectra taken during the first full Martian year of MER operations. Previously, initial results were presented by *Smith et al.* [2004] and *Spanovich et al.* [2006]. Additional analysis of Mini-TES atmospheric observations is given in this issue by *Wolff et al.* [2006].

[1] NASA Goddard Space Flight Center, Greenbelt, Maryland, USA.
[2] Space Science Institute, Boulder, Colorado, USA.
[3] Jet Propulsion Laboratory, Pasadena, California, USA.
[4] Tharsis Inc., Gaithersburg, Maryland, USA.
[5] Department of Astronomy, Cornell University, Ithaca, New York, USA.
[6] Department of Geological Sciences, Arizona State University, Tempe, Arizona, USA.
[7] NASA Glenn Research Center, Cleveland, Ohio, USA.

0148-0227/06/2006JE002770$09.00

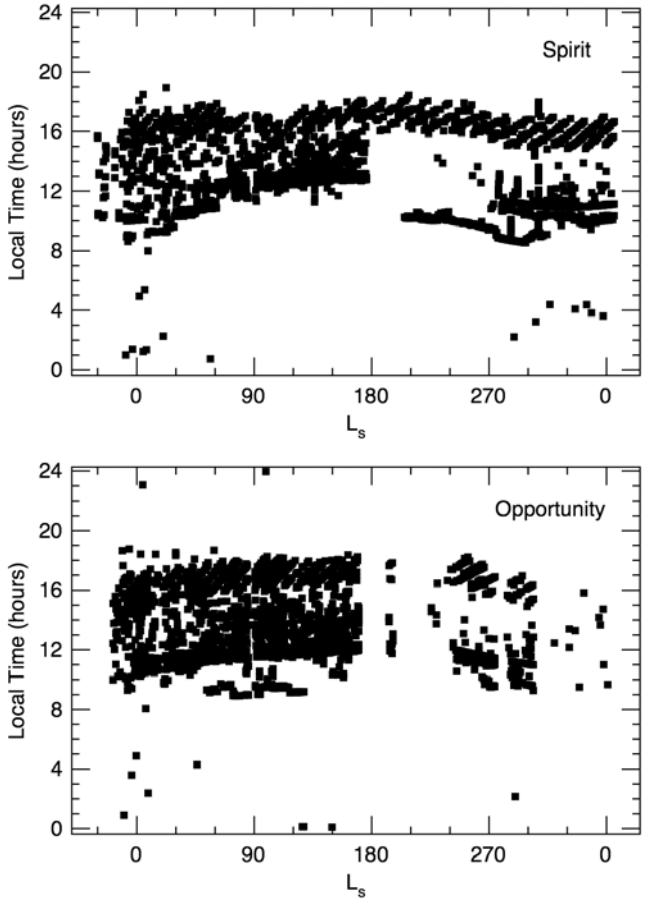

Figure 1. The distribution of Mini-TES upward-looking observations as a function of season (L_s) and local time for (top) Spirit and (bottom) Opportunity.

Atmospheric science using the MER Pancam cameras was presented by *Lemmon et al.* [2004]. In section 2, we discuss the Mini-TES data set and its calibration. Details of the retrieval algorithms are given in section 3. In section 4, we present the results of the retrievals, and those results are discussed in section 5.

2. Data Set

[6] Spirit landed in Gusev Crater (14.6°S, 184.5°W) on 4 January 2004 UTC [*Squyres et al.*, 2004a], or Mars Year 26, L_s = 328°. Opportunity followed three weeks later, landing on Meridiani Planum (1.9°S, 2.5°W) on 24 January 2004 UTC [*Squyres et al.*, 2004b], or Mars Year 26, L_s = 339°. This paper shows the results from retrievals for all atmospheric observations by Mini-TES through 1 February 2006 (Mars Year 28, L_s = 6°) for each rover, covering a little more than a full Martian year at each site. The "Mars Year" convention is from *Clancy et al.* [2000], where Mars Year 1 begins on 11 April 1955. The current Mars Year is 28, which began 21 January 2006.

2.1. Mini-TES Instrument

[7] The Miniature Thermal Emission Spectrometer (Mini-TES) [*Christensen et al.*, 2003] is a Fourier transform spectrometer, and along with the Pancam instrument [*Bell et al.*, 2003], is one of the two primary remote sensing instruments on board the two Mars Exploration Rovers. Mini-TES collects thermal infrared spectra in 167 channels between 339 and 1997 cm^{-1} (5–29 μm) with a spectral sampling of 10 cm^{-1}. The spatial resolution is 20 mrad, and spectra can be acquired every 2 seconds. Mini-TES observes through the top of the Pancam Mast Assembly, which can rotate 360° in azimuth. A pointing mirror allows observations from 50° below to 30° above the plane of the rover deck.

2.2. Observational Strategy

[8] Figure 1 shows the distribution of available upward-looking Mini-TES atmospheric observations taken before 1 February 2006. There are roughly 2200 observations for each rover. Each observation usually contains between 100 and 1000 spectra, so the total number of atmospheric spectra taken by both rovers is approximately one million. Typically, between one and four observations were taken each sol during the nominal daytime hours of rover operation (9:00–18:00 hours local time). Nighttime observations were rare because of the very large energy cost associated with heating of the instrument required for nighttime operation.

[9] Obtaining good coverage in both local time and L_s was always a goal of the atmospheric science group during mission planning, but in practice, constraints from rover operations and competition from other science goals meant that the majority of atmospheric Mini-TES observations were taken either near midday or in the late afternoon. Also apparent in Figure 1 are periods of time when no observations were taken at all. On Opportunity, in the period between L_s = 170° and 240° there are few observations because of technical problems with the Mini-TES instrument and a focus of rover resources to extracting the rover from a sand dune. On Spirit, there are few midday observations between L_s = 180° and 270° because of concerns about getting dust on the instrument optics (see section 2.3.1).

[10] Two main types of upward-looking Mini-TES observations were obtained on a regular basis. The first, called an "elevation scan," took three consecutive sets of 100 spectra at three different elevations angles, which were typically chosen to be 10, 20, and 30 degrees above the plane of the rover deck. Obtaining spectra at three different elevation angles gives three different air masses, which both extends slightly the range in height of sensitivity for the temperature profile retrieval and allows for a more accurate estimation of aerosol and water vapor abundance. Variations of the standard elevation scan included observations with five, seven, or more elevation angles with a smaller spacing between the different angles. The second type of observation, called a "stare," observed the atmosphere at a fixed elevation angle, typically chosen to be as high above the horizon as possible. The duration of these stares ranged from 100 to 1275 consecutive spectra (about 3 to 42 minutes), depending on the resources available. Short-duration stares (e.g., 100 spectra) were taken when only a limited amount of time was available for an observation. Long-duration stares were taken to study the temporal variations of atmospheric temperatures on scales from 2 seconds (i.e., from spectrum to spectrum) to about an hour.

[11] In addition to the above standard observations, there were a few special mini-campaigns to perform coordinated

simultaneous observations with orbital spacecraft during overflights of the rover sites [see *Wolff et al.*, 2006], and to study azimuthal dependence in the atmosphere by taking eight consecutive short stares 45° apart in azimuth.

[12] Along with most of the above upward-looking Mini-TES observations, a short (10 spectra) downward-looking Mini-TES observation was also obtained. The downward-looking observations allow the retrieval of surface temperature and the near-surface atmospheric temperature roughly 1 m above the surface [*Spanovich et al.*, 2006] (also section 3.2). Roughly 1600 downward-looking observations are available for each rover for the time period considered here.

2.3. Calibration

[13] The accurate retrieval of atmospheric parameters from upward-looking Mini-TES observations requires very well-calibrated spectra. Beyond the standard calibration steps described by *Christensen et al.* [2003], we find that there are two additional systematic effects that must be considered to accurately model Mini-TES spectra. The first effect is the accumulation of dust on the instrument optics. Dust can be deposited on the optics as it falls out of the atmosphere or is blown by winds. Winds can also potentially remove dust, although unlike the observed removal of dust from the solar panels [*Landis*, 2005], that appears not to have occurred in any significant amount for the Mini-TES optics. The second systematic effect is a secular change in the instrument response function (IRF). A change in the IRF from the nominal pre-flight value [*Christensen et al.*, 2003] could be caused by repeated "deep sleep" cycles where the rover was allowed to go through the night without survival heaters operating, or by other degradation of the detector or optics.

[14] The systematic effects described here are important. The results of our analysis show that the IRF on Spirit was near unity until about $L_s = 270°$ when it dropped by ~5%, while the IRF on Opportunity has been slowly decreasing over the entire mission. A substantial amount of dust was deposited on the instrument optics of Spirit at $L_s = 172°$ in one event with little other accumulation, while on Opportunity the amount of dust on the optics has increased steadily since early in the mission. Not taking these systematic effects into account can lead to large errors in retrieved atmospheric parameters, especially for Opportunity and for Spirit observations taken after $L_s = 172°$.

2.3.1. Dust on Instrument Optics

[15] The presence of dust on the instrument optics changes the radiance incident on the detector. Some fraction of the radiance from the desired target is absorbed by the dust on the optics and then re-emitted at the temperature of the optics. Presumably, the surface that is coated with dust is the Mini-TES pointing mirror. A simple formulation of this process is given by

$$I^*(\nu) = I(\nu)e^{-\tau_i(\nu)} + \left(1 - e^{-\tau_i(\nu)}\right)B(T_{\text{inst}}, \nu) \qquad (1)$$

where I^* is the radiance including the contribution from the dust (the quantity that reaches the detector and is recorded by the instrument), I is the actual radiance from the scene (the desired quantity), T_{inst} is the temperature of the dust on the instrument, ν is frequency, and $\tau_i(\nu)$ is a measure of the amount of dust on the instrument. If the dust is on the Mini-TES mirror, then T_{inst} is the mirror temperature, which is measured by a temperature sensor and returned as part of each observation. The remaining quantity to be derived is the amount and spectral dependence of the dust, $\tau_i(\nu)$.

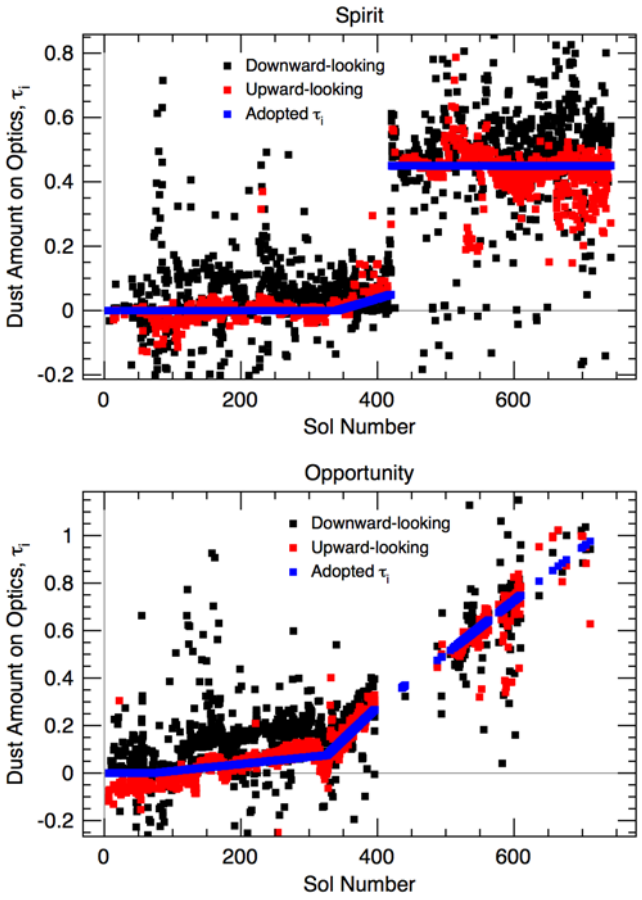

Figure 2. The amount of dust on the instrument optics (τ_i in equation (1)) for (top) Spirit and (bottom) Opportunity. Shown are the best-fit values obtained from downward-looking Mini-TES observations (black), upward-looking Mini-TES observations (red), and the adopted value (blue). Sol number gives the number of sols (Martian days) since landing. Sol number 200 is $L_s = 65°$, sol 400 is $L_s = 165°$, and sol 600 is $L_s = 285°$. There is good agreement between the very different upward- and downward-looking results, indicating that this approach is reasonable. Where there are differences, the adopted value was chosen to more closely follow the best-fit τ_i derived from the upward-looking observations.

[16] There are two independent ways to estimate τ_i. The first is to include the correction given by equation (1) in a radiative transfer least-squares fitting algorithm and then to fit for atmospheric dust optical depth and the amount of dust on the optics (τ_i) in upward-looking Mini-TES spectra. The second way is to model the downward-looking Mini-TES spectra using equation (1) with $I(\nu) = \epsilon(\nu)B(T_{\text{surf}})$ and then fitting for the surface temperature, T_{surf}, and the dust on the optics, τ_i. The surface emissivity, $\epsilon(\nu)$ can be estimated from early-mission data by assuming $\tau_i = 0$.

[17] Figure 2 shows the derived τ_i using both methods as a function of sol (Martian day) for each rover, and the

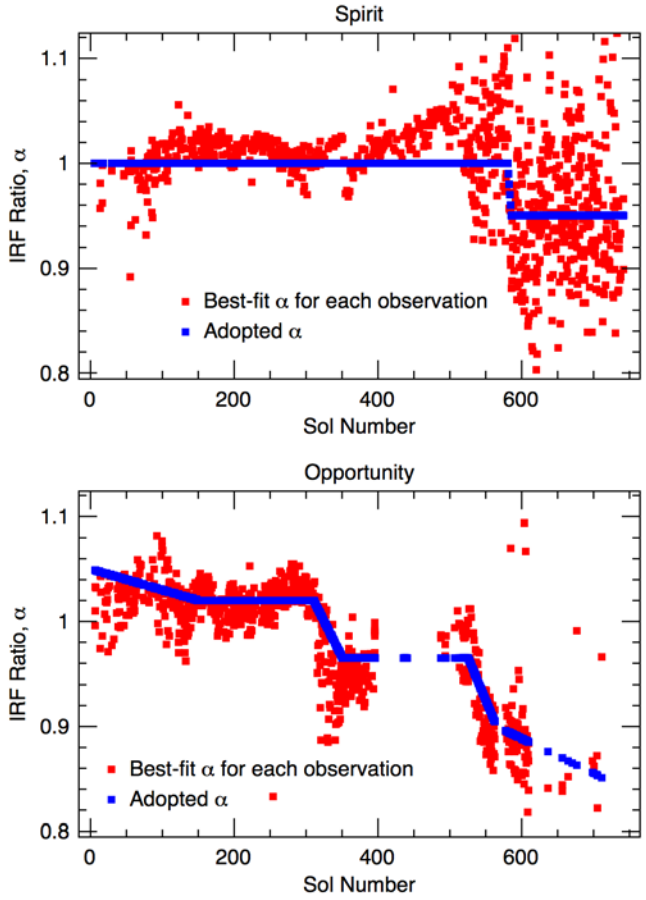

Figure 3. The IRF ratio (α in equation (3)) for (top) Spirit and (bottom) Opportunity. Shown are the best-fit values obtained from upward-looking Mini-TES observations (red) and the adopted value (blue). Sol number gives the number of sols (Martian days) since landing. Sol number 200 is L_s = 65°, sol 400 is L_s = 165°, and sol 600 is L_s = 285°.

adopted form. The results for Spirit are consistent with no dust accumulation until L_s = 140° when the optics began to accumulate a small amount of dust presumably from the large dust storms that began around that time. At L_s = 172°, a single event deposited a substantial amount of dust on the optics. Since that time the amount of dust on the optics has been either constant or very slowly declining. No further events similar to what happened at L_s = 172° have taken place. The results for Opportunity show that dust has been slowly accumulating on the optics since early in the mission and then accelerated around L_s = 140° when atmospheric dust activity suddenly increased. By L_s = 300° there was roughly twice as much dust on the Mini-TES optics of Opportunity as there was on the Mini-TES optics of Spirit.

[18] Given equation (1) and the adopted value of τ_i shown in Figure 2, we can correct for the dust on the optics using

$$I_{\mathrm{corr}}(\nu) = \frac{I_{\mathrm{cal}}(\nu) - \left(1 - e^{-\tau_i(\nu)}\right)B(T_{\mathrm{int}}, \nu)}{e^{-\tau_i(\nu)}} \qquad (2)$$

where I_{cal} is the observed calibrated radiance (including the contribution from the dust on the optics), and I_{corr} is the corrected radiance, as if there were no dust on the optics. This correction has been performed for all the data shown here.

2.3.2. Instrument Response Function

[19] The instrument response function (IRF) is a measure of how much signal the instrument produces for a given input. The IRF is a spectral quantity, and its wavenumber dependence is relatively flat [*Christensen et al.*, 2003]. Because the spectral dependence of the IRF is distinct from dust or the Planck function it can be separated from other effects. We model changes to the IRF through the "IRF ratio", α, defined by

$$\alpha \equiv f_{\mathrm{actual}}/f_{\mathrm{assumed}} \qquad (3)$$

where f is the numerical value of the IRF. It is possible that the spectral dependence of the IRF could change, but the available data do not support anything more than an estimate of the constant multiplicative factor, α. We estimate the IRF ratio, α, by including it within a radiative transfer least-squares fitting algorithm that fits for the IRF ratio along with the other key parameters, the atmospheric dust optical depth and the amount of dust on the optics.

[20] Figure 3 shows the results of the fitting (red points) and the adopted form for the IRF ratio (blue line). For Spirit, the IRF ratio is consistent with unity until around L_s = 270° when there is a drop to α = 0.95. For Opportunity, the IRF ratio began slightly larger than unity, and has dropped throughout the mission to a value of under 0.9 after L_s = 300°.

3. Retrieval Algorithm

[21] After the Mini-TES spectra are calibrated using the IRF ratio shown in Figure 3 and then corrected for dust on the optics using equation (2), we use radiative transfer modeling to retrieve atmospheric temperature as a function of height above the surface, the optical depth of atmospheric dust, and the column abundance of water vapor. Figure 4 shows a sample of typical upward-looking Mini-TES spectra taken by Spirit. The strong emission feature at 600–725 cm^{-1} is used to retrieve atmospheric temperatures, while atmospheric dust provides a broad emission feature throughout most of the spectrum. Water vapor rotation bands are just visible at the lowest frequencies (see also Figure 7).

[22] Although we retain the ability to perform this retrieval on a spectrum-by-spectrum basis, we usually fit for all the spectra in a given observation simultaneously. This decreases noise and gives improved accuracy when multiple elevation angles are present. The retrievals for temperature, dust optical depth, and water vapor column abundance are performed separately, but the sequence is iterated until a self-consistent solution converges.

3.1. Upward-Looking Atmospheric Temperature Retrieval Algorithm

[23] The retrieval of atmospheric temperatures using the upward-looking Mini-TES spectra follows closely the algorithm of *Smith et al.* [1996]. Other previous algorithms for the retrieval of temperatures using thermal infrared spectra of Mars have all been formulated for existing downward-

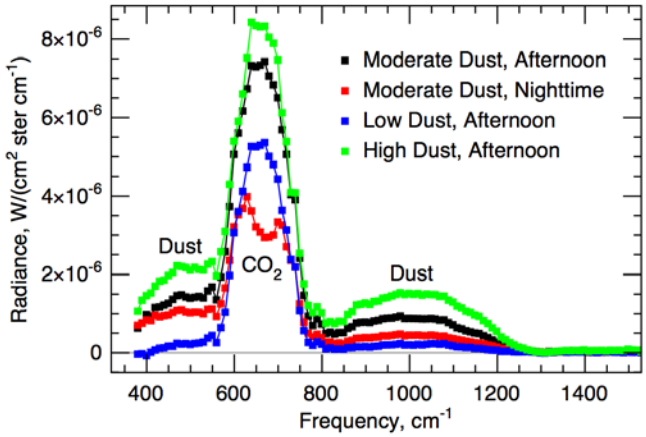

Figure 4. Typical upward-looking Mini-TES observations observed by Spirit. The elevation angles are between 27° and 46° above the plane of the rover deck, and 100 spectra have been averaged in each case. Shown in black is a typical afternoon spectrum (14:12 hours) at L_s = 349° with moderately high dust (τ = 0.42). Shown in red is a typical nighttime spectrum (01:00 hours) at L_s = 351° with moderately high dust (τ = 0.42). Shown in blue is a typical afternoon spectrum (14:35 hours) at L_s = 53° with low dust (τ = 0.08). Shown in green is a typical afternoon spectrum (14:00 hours) at L_s = 171° with high dust (τ = 0.92).

looking spectra taken by orbiting spacecraft [e.g., *Conrath et al.*, 1973, 2000; *Santee and Crisp*, 1993; *Grassi et al.*, 2005). Following *Smith et al.* [1996], the key difference between our upward-looking and previous downward-looking algorithms is a change of variables in the vertical coordinate that gives the weighting functions a functional form that gives the retrieval a more mathematically stable form.

[24] The weighting function, W is given by

$$W(\nu, s) = \frac{\partial}{\partial s}\left[e^{-\tau(\nu,s)}\right] \tag{4}$$

where $\tau(\nu, s)$ is the optical depth (of CO_2 gas in this case), s is the coordinate that describes distance along the line of sight, and ν is frequency. The weighting function describes where the observed radiation originates along the viewing path, and it is a function both of the frequency, ν, and the distance coordinate, s. A retrieval algorithm has best performance when the weighting functions for different frequencies are distinct and have peak amplitude at different values of s.

[25] In the downward-looking geometry (from orbit) the above conditions are obtained by choosing s to measure distance in scale heights above the surface. However, in the upward-looking geometry (from the surface) that choice for s gives weighting functions that are all sharply peaked at the surface with little difference in shape between different frequencies. The choice of coordinate suggested by *Smith et al.* [1996] of

$$s(p) = \ln\left[\frac{p_{\text{surf}} - p}{p_{\text{surf}}}\right] \tag{5}$$

where p is atmospheric pressure, p_{surf} is the surface pressure, and "ln" is the natural logarithm function, gives well separated weighting functions with peaks at different heights above the surface by stretching out the coordinate close to the surface. Figure 5 shows a typical set of weighting functions for Mini-TES with this vertical coordinate. The weighting functions also show the range in height where the retrieval is sensitive to temperatures. Above 2 km, the weighting functions all decrease monotonically with similar shapes, while the lowest weighting function peaks at about 15 m above the surface. Thus we take the vertical range of validity to be 15–2000 m for the temperature profiles retrieved from upward-looking Mini-TES spectra.

[26] The actual retrieval is performed using a constrained, linear least-squares inversion [*Conrath et al.*, 1994], the step-by-step mathematics of which is given by *Smith et al.* [1996]. The constraints take the form of a low-pass filter in the vertical coordinate that acts to smooth the temperature profile. The tradeoff here is between increased vertical resolution and decreased temperature uncertainty [*Conrath*, 1972]. The balance is struck by varying parameters until a maximum vertical resolution is obtained while retaining an acceptable temperature uncertainty.

[27] The radiative transfer used in the retrieval computes CO_2 gas absorption using the correlated-k approach [e.g., *Lacis and Oinas*, 1991; *Goody et al.*, 1989] with line parameters from the HITRAN 2004 spectroscopic database [*Rothman et al.*, 2005]. Opacity from dust aerosol is also included, but is not retrieved simultaneously (see section 3.2). An important parameter that is necessary to compute CO_2 gas absorption is the surface pressure since that gives the total mass of CO_2 above the rover. However, there is no pressure sensor on board MER and the Mini-TES spectra themselves are not of sufficient spectral resolution to retrieve the surface pressure to better than perhaps ~30%. Therefore we have used the results of numerical modeling of R. M. Haberle and R. J. Wilson (personal communication, 2003) to estimate surface pressure as a function of L_s and local time for the two rover sites. We have fit the modeling results of Haberle and Wilson for Spirit as

$$\begin{aligned} p_{\text{surf}}(L_s, t) = {} & 6.917 + 0.342\cos[L_s - 333] + 0.377\cos[2(L_s - 75)] \\ & + 0.076\cos[3(L_s - 11)] + 0.044\cos[4(L_s - 68)] \\ & + 0.189\cos[360(t/24 - 0.26)] \\ & + 0.057\cos[720(t/24 - 0.40)]\ \text{mbar} \end{aligned} \tag{6a}$$

and Opportunity as

$$\begin{aligned} p_{\text{surf}}(L_s, t) = {} & 6.682 + 0.355\cos[L_s - 340] + 0.430\cos[2(L_s - 76)] \\ & + 0.079\cos[3(L_s - 12)] + 0.047\cos[4(L_s - 68)] \\ & + 0.193\cos[360(t/24 - 0.26)] \\ & + 0.059\cos[720(t/24 - 0.41)]\ \text{mbar} \end{aligned} \tag{6b}$$

where t is local time measured in hours, with 24 hours in a sol.

[28] The temperature retrieval algorithm also requires a first guess temperature profile. We use climatological averages of atmospheric temperature as a function of height as

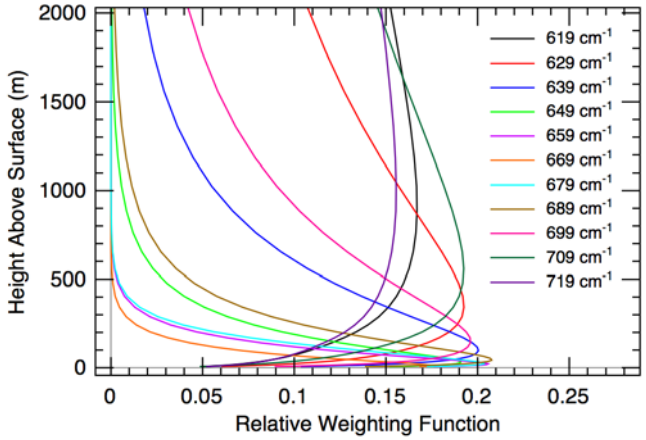

Figure 5. Weighting functions for the frequencies used in the retrieval of atmospheric temperatures from upward-looking Mini-TES spectra. The transformation to the vertical coordinate given in equation (5) has been performed. With that choice, the weighting functions have well-defined peaks at different heights above the surface. The Mini-TES temperature retrieval has sensitivity between 15 and 2000 m above the surface with a high vertical resolution near the surface and lower vertical resolution near the top of the domain.

retrieved from TES observations [*Smith*, 2004, 2006]. As shown in section 3.5, in the vertical range where the Mini-TES retrieval is valid (15–2000 m above the surface), the retrieved temperature profiles are not very sensitive to the initial guess or the estimated surface pressure, especially near the surface.

3.2. Aerosol Optical Depth Retrieval Algorithm

[29] Aerosol optical depth is retrieved by minimizing the least-squares difference between the observed Mini-TES spectrum outside the 15-μm CO_2 band and a synthetic spectrum. The synthetic spectrum is computed using a two-stream radiative transfer code that includes aerosol scattering [e.g., *Goody and Yung*, 1989; *Thomas and Stamnes*, 1999]. It is important to include scattering for the upward-looking geometry because the wide range of surface temperatures encountered (even within the nominal "daytime" Mini-TES coverage) provides an important and variable source for scattered radiation. We have estimated the spectral dependence of the extinction cross section, $Q_{ext}(\nu)$, and the single-scattering albedo, $\varpi_0(\nu)$, for dust using the Mini-TES observations themselves by performing a least-squares fit to find the single form of $Q_{ext}(\nu)$ and $\varpi_0(\nu)$ that best fits the Mini-TES observations taken early in the mission when we expect only dust to be present. Figure 6 shows the best-fit extinction cross section and single-scattering albedo. It is similar to previously determined dust scattering properties [e.g., *Bandfield and Smith*, 2003; *Wolff and Clancy*, 2003] and to the scattering properties derived by *Wolff et al.* [2006] from the Mini-TES spectra. Water ice aerosol scattering properties were taken from *Wolff and Clancy* [2003].

[30] Three key simplifying assumptions enter into the retrieval of aerosol optical depth. First, upward-looking Mini-TES observations of aerosols sample the entire column of atmosphere outside the CO_2 band, but Mini-TES temperature retrievals are only sensitive to the lowest 2 km of the atmosphere. Therefore we use TES climatological averages [*Smith*, 2004, 2006] for the temperature profile above a height of 2 km. The uncertainties in retrieved optical depth are discussed in section 3.5.

[31] The second assumption is that the dust aerosols are well-mixed. Previous experience with Viking [*Pollack et al.*, 1977; *Jaquin et al.*, 1986], Pathfinder [*Smith et al.*, 1997], and TES [*Smith*, 2003] indicate that this is a reasonable assumption. Direct imaging of the Sun near the horizon using the MER Pancam instrument [*Lemmon et al.*, 2004] also supports the well-mixed approximation. A further discussion of the vertical distribution of dust is given by *Wolff et al.* [2006]. On the other hand, ice aerosols are not treated as well-mixed. The water condensation level is computed, and water ice clouds are restricted to the atmosphere above the condensation level.

[32] The third assumption is that a single spectral form for the extinction cross section and single-scattering albedo (Figure 6) is valid for both rovers and for all seasons. Using Mini-TES observations, *Wolff et al.* [2006] report small changes in the effective size of dust aerosols as a function of time which would lead to small changes in the extinction cross section and single-scattering albedo. However, those changes lead to small changes in retrieved dust optical depth and do not affect the character of the seasonal trends presented here.

3.3. Water Vapor Retrieval Algorithm

[33] Water vapor is retrieved in a third step separately from the temperature profile and aerosol optical depth. The three retrievals are then iterated sequentially until the retrieved values converge to a self-consistent solution. Although the spectral coverage of Mini-TES does not include the stronger water vapor rotational bands at 240–350 cm^{-1} that were used by *Smith* [2002] to retrieve water vapor column abundance from TES spectra, there are still

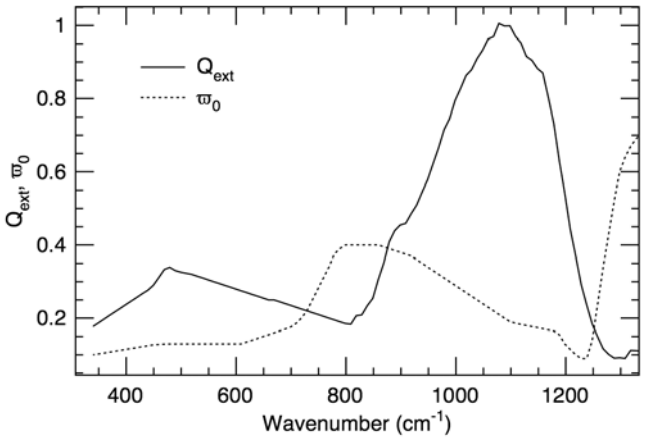

Figure 6. The extinction cross section, Q_{ext}, and single-scattering albedo, ϖ_0, for dust aerosols derived from Mini-TES observations and used in the retrieval of dust optical depth.

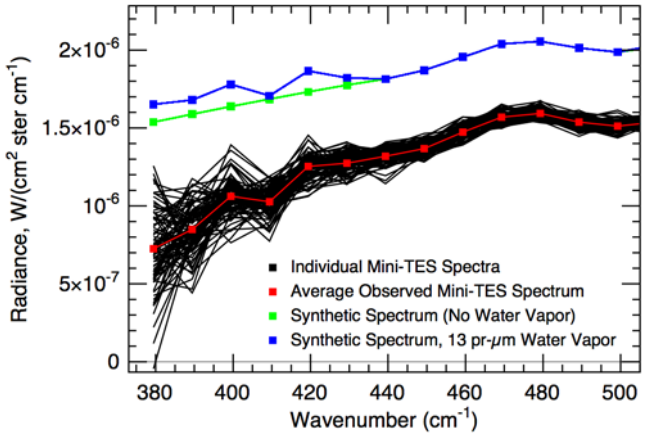

Figure 7. The observation of water vapor in upward-looking Mini-TES spectra. The black lines show the 100 individual spectra observed by Spirit at 14:12 hours at L_s = 349°. The red line with points shows the average of the 100 spectra. This is the same spectrum shown in Figure 4. The green line shows a synthetic spectrum without water vapor, while the blue line shows the same synthetic spectrum with 13 pr-μm water vapor (the two synthetic spectra have been offset for clarity). Water vapor shows up as a pair of peaks at 400 and 420 cm^{-1}.

weaker water vapor rotational bands at 380–440 cm^{-1} that are visible in Mini-TES upward-looking spectra.

[34] Figure 7 shows a typical Mini-TES observation of water vapor. The 100 individual spectra (shown in black) show a systematic pair of weak emission peaks at 400 and 420 cm^{-1}, which show up more clearly in the average (red line). A synthetic spectrum with a column abundance of 13 precipitable microns (blue line) shows the same pair of peaks with the same amplitude. The retrieval algorithm simply varies water vapor column abundance until the strength of the spectral features at 400 and 420^{-1} match those in the observation. Water vapor absorption is computed using the correlated-k approximation, with line strengths and other parameters taken from the HITRAN 2004 spectroscopic database [*Rothman et al.*, 2005]. Following *Smith* [2002], line broadening from CO_2 is approximated by multiplying the terrestrial air broadening coefficients from HITRAN 2004 by a constant factor of 1.5.

3.4. Downward-Looking Temperature Retrieval Algorithm

[35] Figure 8 shows typical downward-looking Mini-TES spectra. Because the path length through the atmosphere is only about 4 m in this geometry, there is very little contribution from the atmosphere other than in the center of the 15-μm CO_2 band (667 cm^{-1}). Although not opaque at the Mini-TES spectral resolution, the CO_2 absorption is still strong enough to provide meaningful information about atmospheric temperatures along the path. Following *Spanovich et al.* [2006], we model the observed radiance using a single atmospheric layer using:

$$I = \epsilon(\nu)B(T_{\text{surf}},\nu)e^{-\tau} + B(T_{\text{atm}},\nu)(1-e^{-\tau}) \qquad (7)$$

where ϵ is surface emissivity, B is the Planck function at frequency ν and either the surface temperature, T_{surf} or the near-surface atmospheric temperature T_{atm}, and τ is the atmospheric optical depth (from CO_2) along the path. The ~4 m atmospheric path length of these observations is too short for atmospheric dust to contribute to the atmospheric optical depth, τ, so no information about atmospheric dust is retrieved from the downward-looking Mini-TES spectra.

[36] We are more interested in accounting for the entire first term of equation (7) (the contribution from the surface), than in fitting for an accurate surface temperature, so it is sufficient for our purpose to simply approximate the surface emissivity, ϵ, as unity and to let the surface temperature in equation (7) be an effective value. The height of the rover mast (1.5 m) and geometry of the observation are well-known, so the optical depth of CO_2 can easily be computed using the correlated-k approximation using the approximation for surface pressure given in equation (6a) (6b) above. The remaining parameters, the effective surface temperature and the near-surface atmospheric temperature are fit minimizing the least-squared difference between computed and observed radiance between 600 and 740 cm^{-1}, which includes both the CO_2 feature (to constrain T_{atm}) and the continuum outside the CO_2 band (to constrain T_{surf}). Numerical experiments [*Spanovich et al.*, 2006] show that the retrieved near-surface temperature, T_{atm}, is indicative of a height approximately 1.1 m above the surface.

3.5. Estimated Uncertainties

[37] The formal uncertainty calculated from the propagation of instrument noise [*Christensen et al.*, 2003] leads to relatively small uncertainties in both temperature (<1 K) and aerosol optical depth (<0.02) [*Smith et al.*, 2004]. Of greater relevance are the uncertainties related to systematic errors in the calibration and retrieval algorithm. For example, Figure 9 shows the sensitivity of the retrieved temperature

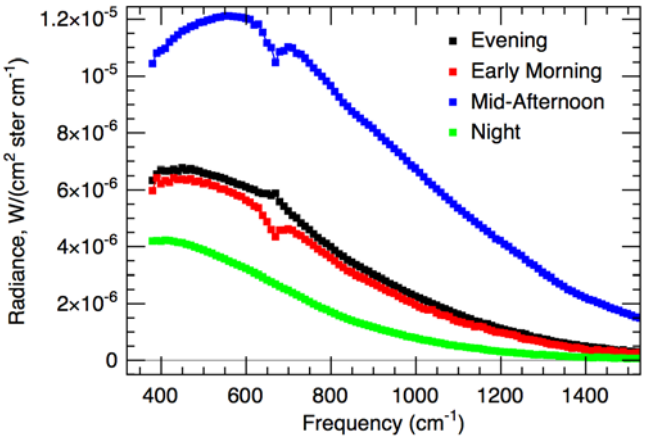

Figure 8. Typical downward-looking Mini-TES observations observed by Spirit. Ten spectra have been averaged in each case. Shown in black is a typical evening spectrum (17:29 hours) at L_s = 355°. Shown in red is a typical early morning spectrum (08:48 hours) at L_s = 356°. Shown in blue is a typical midafternoon spectrum (14:17 hours) at L_s = 349°. Shown in green is a typical nighttime spectrum (00:55 hours) at L_s = 351°.

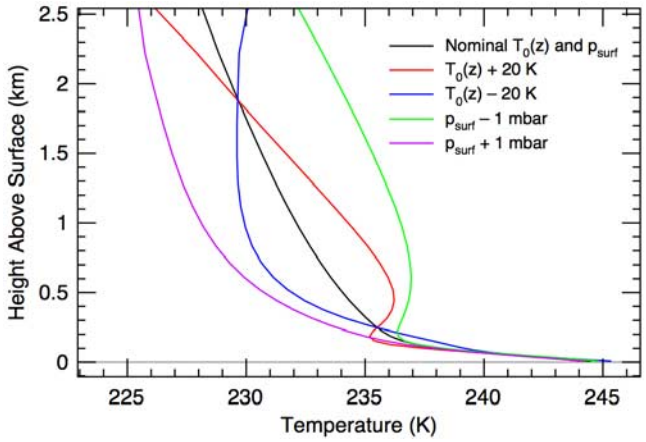

Figure 9. Sensitivity of the temperature retrieval to changes in the assumed surface pressure, p_{surf}, and the first-guess temperature profile, $T_0(z)$. The nominal retrieval is shown in black. The red and blue curves show the effect of adding and subtracting a constant 20 K offset to the assumed nominal first-guess temperature profile. The green and purple curves show the effect of adding and subtracting 1 mbar from the assumed nominal surface pressure. The retrieval is fairly robust to changes in these parameters.

profile to changes in the assumed surface pressure, p_{surf}, and first-guess temperature profile, $T_0(z)$. The black line shows the temperature profile retrieved with nominal p_{surf} and $T_0(z)$, while the colored lines show temperatures retrieved when the surface pressure is varied by 1 mbar or the first-guess temperature profile is shifted by 20 K (constant with height). These variations are much larger than the expected uncertainty in the estimates for p_{surf} and $T_0(z)$, so they give a conservative estimate of the largest expected uncertainty from these two assumptions. Near the surface (below about 200 m), the error is less than 1 K, while at higher above the surface the errors increase to as large as 5 K. On the basis of numerical experiments such as these, and our experience with similar retrieval algorithms on previous missions [e.g., *Conrath et al.*, 2000; *Smith et al.*, 2004], we estimate the uncertainty in retrieved temperature to be 2 K near the surface (lower than 200 m), increasing to 4 K at the upper level of sensitivity (2 km).

[38] A similar analysis of numerical experiments and propagation of errors can be performed for estimating the uncertainties in aerosol optical depth and water vapor column abundance. For aerosol optical depth, the largest uncertainty comes from the assumption of a temperature profile above the 2 km height accessible to the temperature retrieval. Numerical experiments show that a 10 K shift in the assumed temperature profile results in errors in retrieved optical depth no greater than 10%. We estimate the total uncertainty in aerosol optical depth to be the larger of 0.03 or 10%. Uncertainty in the retrieval of water vapor column abundance has significant contributions from the temperature profile above 2 km, the surface pressure estimate, poor knowledge of the magnitude of CO_2 broadening of water vapor, and the noise in the observations themselves, which as can be seen in Figure 7 rises rapidly at the lowest wavenumbers where the water vapor bands are located. Combining all these contributions, we estimate an uncertainty of 5 precipitable microns (pr-μm).

4. Results

[39] Here we present results from the retrieval of atmospheric temperature, dust optical depth, and water vapor column abundance from the Mini-TES observations. The retrievals presented here cover just over one Martian year of observations, from landing until 1 February 2006. Unless otherwise indicated, the retrievals were all performed by fitting all the spectra within a single observation, which can contain anywhere between 100 to 1275 spectra in the upward-looking geometry, and between 5 and 255 spectra in the downward-looking geometry.

4.1. Characteristics of Atmospheric Temperature Profile

[40] Figure 10 shows a typical sample of temperature profiles retrieved from Spirit. *Smith et al.* [2004] previously showed a similar sample of temperature profiles. Upward-looking Mini-TES spectra provide useful information on atmospheric temperatures between about 15 and 2000 m above the surface. The vertical resolution of the retrievals is better than 100 m near the surface, decreasing rapidly to about 1 km at the top of the domain. It should also be noted that because Mini-TES can view no more than 30 degrees above the plane of the rover deck, the atmosphere that is sensed becomes increasing far away horizontally from the rover as height is increased. For example, at 30 degrees elevation angle, temperatures 1 km above the surface are sampled from 2 km away from the rover horizontally. This effect is not so much a case of horizontal averaging as much as the fact that temperature profiles presented here are representative of temperatures along the line-of-sight, rather than temperatures directly above the rover.

[41] The temperature profiles shown in Figure 10, which were all taken within 4 days of each other, show the wide range of conditions experienced by the rover during the course of a day. At night (black and red lines), a strong

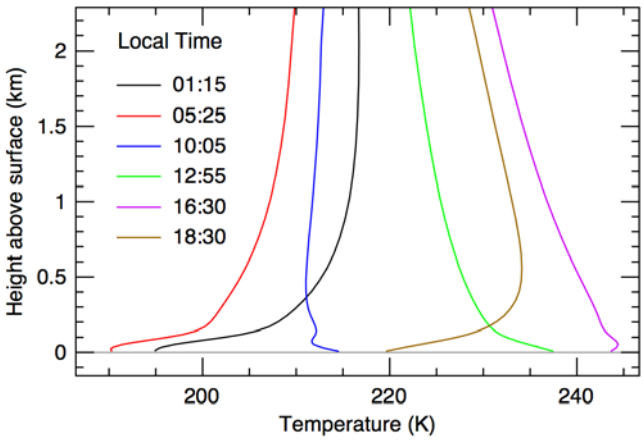

Figure 10. Typical temperature profiles retrieved from upward-looking observations made over the course of four days by Spirit near L_s = 5°. The evolution of the daytime near-surface superadiabatic layer and the nighttime inversion layer is evident.

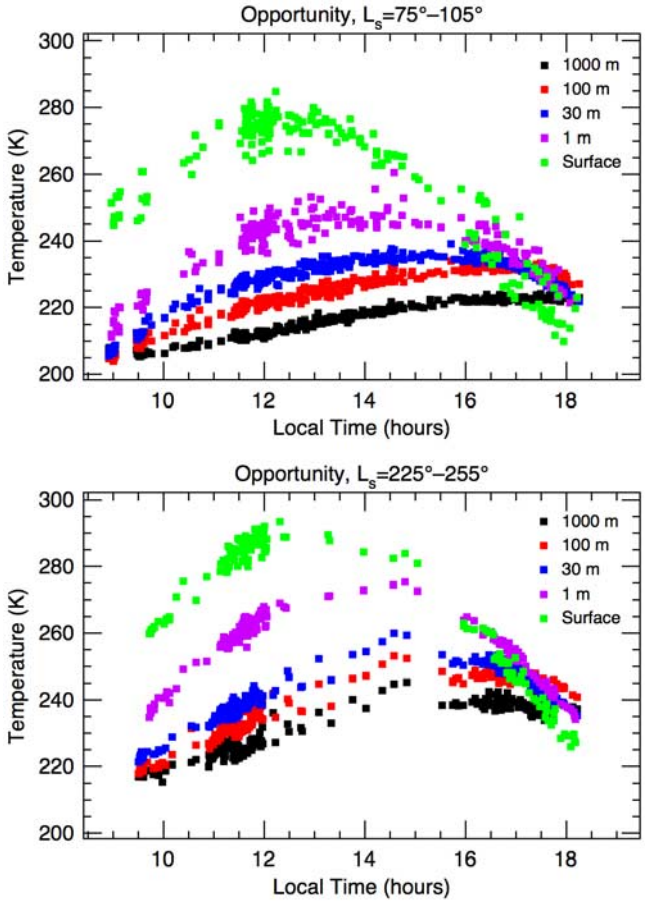

Figure 11. Temperature as a function of local time as observed by Opportunity. The top panel shows temperatures during the aphelion season (L_s = 75°–105°); the bottom panel shows temperatures during the perihelion season (L_s = 225°–255°). Effective surface temperature (assuming unit surface emissivity) and atmospheric temperature at 1 m height are retrieved from downward-looking Mini-TES observations. Atmospheric temperatures at 30, 100, and 1000 m above the surface are retrieved from upward-looking Mini-TES observations.

inversion layer develops, extending to more than 1 km in height with an amplitude of tens of degrees. Soon after sunrise, the inversion layer disappears, and by 10:05 (blue line) is replaced by the beginnings of a superadiabatic lapse rate near the surface. By midday (green line), the superadiabatic layer is well-formed, reaching 100–200 m above the surface with gradients well in excess of the adiabatic lapse rate. This persists until early evening (purple line), when the superadiabatic layer is once again replaced by an inversion layer after the sun sets (brown line).

[42] The main feature of the daytime temperature profiles is the strong gradient of temperature near the surface. In this layer, which extends to 100–200 m above the surface, convective motions within the thin Martian atmosphere cannot transport sufficient heat from the surface layer to maintain an adiabatic lapse rate. An unstable, superadiabatic layer results, which develops midmorning and persists until late afternoon. Superadiabatic lapse rates have previously been observed near the surface by Pathfinder [*Schofield et al.*, 1997] and have been modeled [e.g., *Savijärvi et al.*, 2004; *Michaels and Rafkin*, 2004].

[43] All the temperature profiles retrieved from Mini-TES are variations of one of the basic types shown in Figure 10. Although there are real fluctuations in the temperature structure with amplitude of a few degrees (see section 4.6) that occur over timescales of less than a minute, at the vertical resolution of the Mini-TES retrieval these are not great enough to alter the basic form of the temperature profile shown here. For example, we do not see any daytime temperature inversions or other large-scale variations in the temperature profiles.

4.2. Diurnal Cycle of Atmospheric Temperatures

[44] The variation of retrieved atmospheric and effective surface temperature as a function of local time at the Opportunity landing site is shown in Figure 11 for aphelion (top panel) and perihelion conditions (bottom panel). Only daytime hours are shown because no nighttime Mini-TES observations were taken by Opportunity between L_s = 225° and 255°, and only one was taken between L_s = 75° and 105°. The effective surface temperature and the atmospheric temperature at 1 m height were derived from downward-looking spectra, while the atmospheric temperatures at 30, 100, and 1000 m height were derived from upward-looking spectra.

[45] Apparent in Figure 11 is the increase of the superadiabatic lapse rate during the morning hours and its rapid decrease after 16:00 hours. The temperature difference between 1 and 100 m reaches a maximum of about 20 K in the aphelion season and about 30 K in the perihelion season, which can be compared to the adiabatic lapse rate of 4.5 K/km. The maximum lapse rate occurs between 12:00 and 13:00 hours local time. Temperatures at 1 and 100 m height are the same at 17:30 hours and become inverted after that. The temperature difference between 100 and 1000 m height reaches about 8 K between 12:00 and 17:00 hours local time in both seasons, which is still superadiabatic.

[46] There is a notable lag in the time of maximum diurnal atmospheric temperature compared to surface temperature. While surface temperatures reach a maximum near the maximum solar input at 12:00 local time, atmospheric temperatures, driven by a combination of radiation and sensible heat flux, continue to increase for several more hours reaching a diurnal maximum at about 14:00 hours at 1 m above the surface and about 16:30 at 1000 m. The time of maximum diurnal atmospheric temperature becomes increasingly later for greater heights above the surface. There appears to be little difference in the time of maximum diurnal temperature between the aphelion and perihelion seasons.

4.3. Seasonal Trends in Temperatures

[47] Figure 12 shows the variation in atmospheric temperatures at the Spirit landing site as a function of season (L_s) for three different heights above the surface (top panel) and three different times of day (bottom panel). Because both rovers are located near the equator, PBL temperatures are driven more by solar insolation differences between aphelion (L_s = 71°) and perihelion (L_s = 251°) than differences between summer and winter. At the Spirit landing site, the

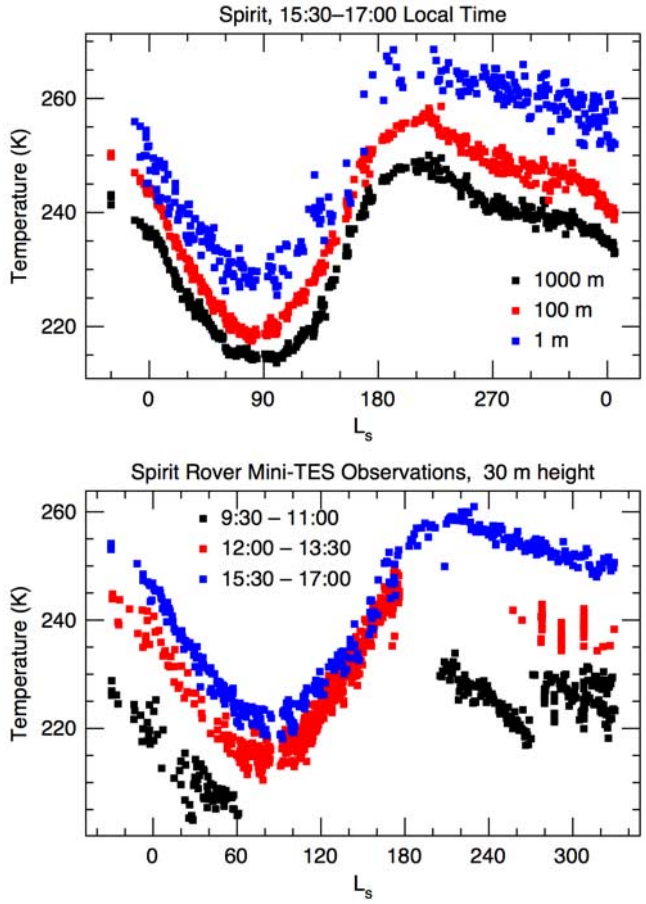

Figure 12. The seasonal dependence of temperatures observed by Spirit. The top panel shows atmospheric temperature at three different heights. The 1 m temperatures are retrieved from downward-looking observations. The 100 and 1000 m temperatures are retrieved from upward-looking observations. The bottom panel shows temperatures 30 m above the surface at three different local times, with morning observations in black, midday observations in red, and late afternoon observations in blue.

maximum annual atmospheric temperature was recorded at roughly L_s = 220° for all heights and times of day. Minimum annual atmospheric temperatures were reached near L_s = 85°. The annual cycle of temperatures is not symmetrical, with a relatively rapid increase in temperatures between L_s = 120° and 180° followed by a relatively slow decrease in temperatures between L_s = 240° and 360° and a more rapid decrease between L_s = 0° and 60°. These same trends were also observed in TES data from the lower atmosphere (3.7 mbar) [*Smith et al.*, 2004].

[48] The amplitude of the temperature difference between 100 and 1000 m height mirrors the temperatures themselves, with a minimum value of about 4 K near L_s = 80° and a broad maximum of about 7 K during the entire period between L_s = 140° and 340°. On the other hand, the amplitude of the temperature difference between 1 and 100 m height does not show the same seasonal pattern, but instead drifts slowly upward from roughly 8 K at the beginning of the mission to 14 K in the most recent data shown. This upward drift is almost certainly caused by an imperfect correction of the systematic calibration effects described earlier (section 2.3) between the upward- and downward-looking spectra. However, the lack of any other seasonal signal in the lapse rate in the lowest 100 m appears to be real.

[49] There is no obvious seasonal trend to the difference between 30-m temperatures at different times of day. All of variations seen in the bottom panel of Figure 12 can be explained by systematic changes in the local time of observations within the 90-minute windows shown. Referring back to Figure 1, the narrowing of difference between midday (red points) and late-afternoon (blue points) temperatures between L_s = 90° and 180° is caused by a corresponding systematic drift toward later local time (and thus a relatively warmer time of the day) during that period for the midday points. Likewise, the sudden "jump" in the morning temperatures (black points) near L_s = 270° is caused by a jump in the observations to later local times. The three vertical bars in the midday temperatures between L_s = 270° and 310° are the result of near-continuous observations across the local time span (12:00 to 13:30). Once those effects are taken into account it can be seen that there are no large changes in the morning-to-afternoon temperature difference as a function of season.

4.4. Seasonal Trends in Aerosol Optical Depth

[50] Figure 13 shows the seasonal variation of dust optical depth at the Spirit and Opportunity landing sites. All dust optical depth values quoted here and shown in the figures are the normal-incidence column dust optical depth from the surface to infinity at 1075 cm^{-1}. Dust optical depth at the rover sites has also been retrieved in a separate analysis of Mini-TES upward-looking spectra [*Wolff et al.*, 2006] and by direct imaging of the Sun by the Pancam instrument [*Lemmon et al.*, 2004].

[51] The two rovers landed during the decay of a large regional dust storm that began in mid-December 2003, which was observed by TES and Mars Odyssey THEMIS [*Smith et al.*, 2004; *Smith*, 2006]. The highest dust optical depth during the active part of the storm was at low southern latitudes between 0° and 60°W longitude (just south and west of the Opportunity landing site). The dust storm began to dissipate in the last week of December 2003 and by mid-January 2004, the active part of the dust storm was over and there was little remaining longitude variation at low latitudes.

[52] Both rovers recorded the decay of the regional dust storm and general clearing associated with the transition to the aphelion season [*Smith et al.*, 2004]. Minimum annual dust optical depth of roughly 0.25 was reached at L_s = 30° at Opportunity, while the dust optical depth at Spirit continued to drop to about 0.1 at L_s = 50°. The low dust optical depth values persisted throughout the aphelion season until L_s = 140° when dust activity dramatically returned at both sites at a seasonal date earlier than expected from observations from previous years. Between L_s = 140° and L_s = 330° a series of dust storms periodically raised dust optical depth at each site to near (or even above) unity for short periods of time. Between dust storms, the dust optical depth retained a high "background" value of about 0.25–0.3, typical of the perihelion season at these locations. Overall, the Mars

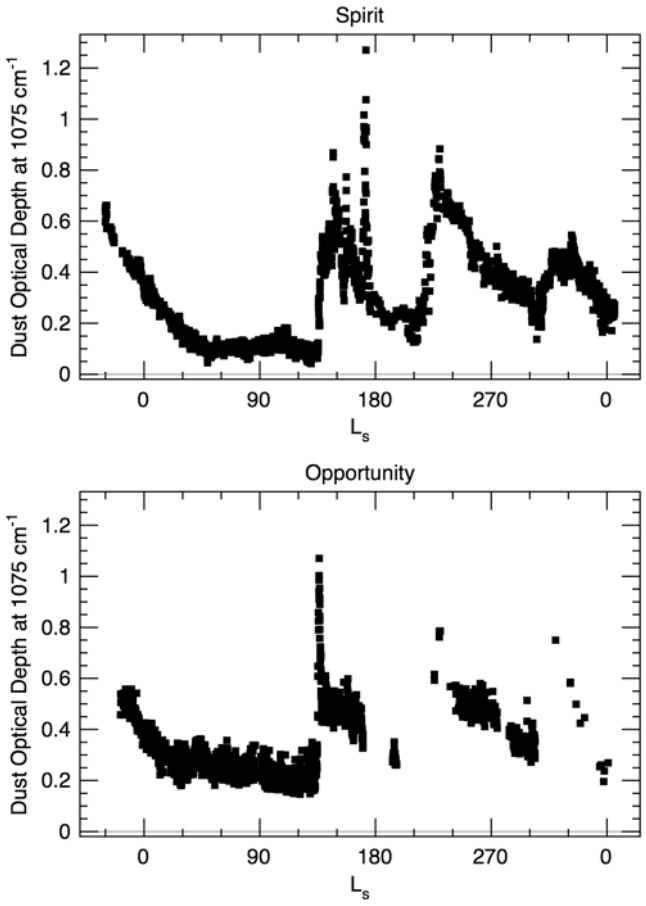

Figure 13. Dust optical depth as a function of season for (top) Spirit and (bottom) Opportunity. Shown is the normal-incidence dust optical depth at 1075 cm^{-1} from the surface to infinity.

Year 27 dust storm season observed by the rovers was quite moderate, with no global-scale planet-encircling dust storms of the magnitude of the 2001 storm (Mars Year 25) [*Smith et al.*, 2002].

[53] The value of having multiple operational rovers on the surface at the same time is clear from comparing the seasonal history of dust activity at the two rover sites located 180° in longitude away from each other. Small local dust storms will be viewed by one rover, but not by the other. Winds will advect the enhanced dust away and the observed increase in dust optical depth lasts only days. The effect of large, regional dust storms will be observed at both rover sites. In this case, because a large portion of the planet at low latitudes has increased dust, winds cannot easily advect dust away. The observed dust optical depth can only fall by dust settling, which typically has a timescale of a couple months [e.g., *Conrath*, 1975; *Smith et al.*, 2000]. Several examples of each type of dust storm are seen in the record shown in Figure 13. Large, regional-scale dust storms began at L_s = 140°, 220°, and 310°. Small, local-scale dust storms were observed by Spirit at L_s = 157°, 170°, and 275°, and at Opportunity at L_s = 298°.

4.5. Seasonal Trends in Water Vapor Abundance

[54] The column-integrated water vapor abundance retrieved for each upward-looking Mini-TES observation is shown in Figure 14. Shown is the normal-incidence abundance from the surface to infinity. The column abundances retrieved from each individual observation are shown as the black points. Because of the noisy nature of the retrieved values, a red line giving a smoothed representation of the retrievals is also shown. For comparison, the blue points show the water vapor column abundance retrieved from TES observations during the previous martian year as recorded in the TES climatology database [*Smith*, 2006].

[55] The retrievals from observations made by Spirit show a clear seasonal pattern. Water vapor abundance decreased from the time of landing until L_s = 50°, remained at low levels (less than 5 pr-μm) until L_s = 160°, increased rapidly to near 20 pr-μm at L_s = 200°, and then slowly decreased back below 10 pr-μm by L_s = 330°. This seasonal pattern is generally consistent with the TES observations,

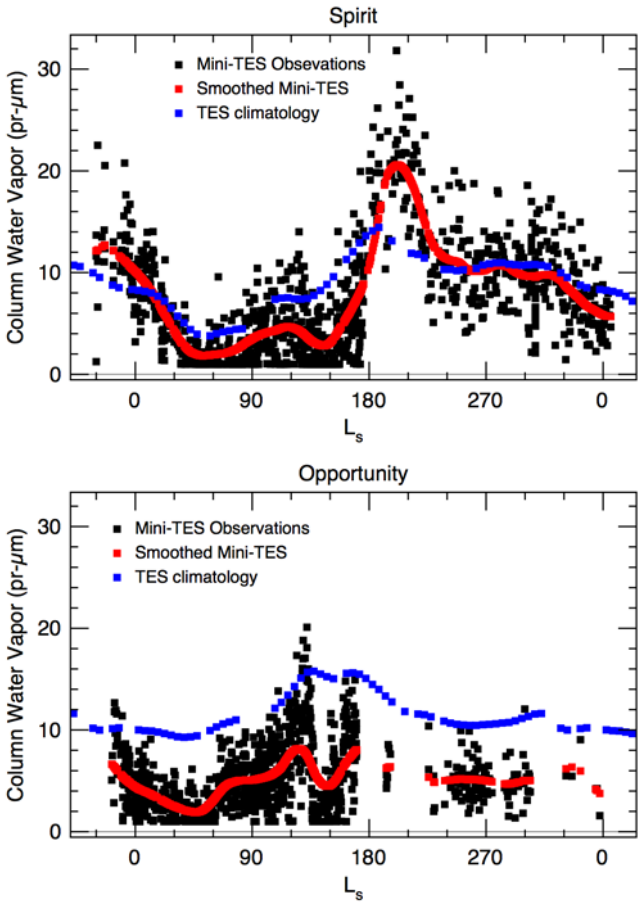

Figure 14. Water vapor column abundance as a function of season for (top) Spirit and (bottom) Opportunity. Shown is the normal-incidence column-integrated value from the surface to infinity in precipitable-microns (pr-μm). The black points show the retrieved values from individual Mini-TES observations. The red points show a smoothed representation of the individual retrievals. The blue points show the water vapor abundance taken from TES climatology.

which also show seasonal minimum and maximum values at the same times and with similar abundances. The seasonal trend of water vapor abundance has some similarities with the seasonal trend of dust optical depth (Figure 13), but the dust activity started well before the rise in water vapor, and the seasonal trend of water vapor has a single peak while the seasonal trend of dust optical depth has several comparable peaks.

[56] The retrievals from observations made by Opportunity also show seasonal variation. An initial decline in water vapor column abundance to well below 5 pr-μm at $L_s = 50°$ was followed by a gradual rise to a broad peak (or perhaps double peak) of about 10 pr-μm at $L_s = 120°$ to 180°, which was followed by a slow decline for the remainder of the year. This seasonal behavior, including the earlier seasonal date for the maximum abundance compared to the Spirit landing site, is consistent with the seasonal trend observed by TES. However, the water vapor column abundance retrieved from Opportunity is systematically only about half as large as TES observations would indicate. The reason for this difference is not known. The lower water vapor observed by Opportunity may be caused by local phenomena since the values from TES climatology are averaged over a fairly large region a few hundred km in size.

4.6. Short Timescale Variations

[57] One of the more intriguing results from the Mini-TES atmospheric observations becomes apparent when the temperature profiles are retrieved on a spectrum-by-spectrum basis rather than averaging all spectra for a given observation as reported above. Turbulent motions associated with convection are observed in the upward-looking Mini-TES retrievals to create large (up to 5 K) temperature fluctuations on timescales of 15–60 seconds. Similar temperature fluctuations with even greater amplitude (up to 8 K) are observed at 1 m above the surface in the downward-looking Mini-TES retrievals [*Spanovich et al.*, 2006]. Large-amplitude, short timescale temperature fluctuations have previously been observed by the Pathfinder and Viking landers during daytime hours [*Hess et al.*, 1977; *Schofield et al.*, 1997].

[58] Figure 15 shows examples of the temperature fluctuations. A temperature profile is retrieved from each Mini-TES spectrum giving an observation every 2 seconds. At each height the time-averaged temperature is subtracted leaving the time-variable portion of the thermal field. In Figure 15, average temperatures are shown as green, while warmer than average temperatures are yellow and red, and cooler than average temperatures are blue and purple.

[59] The top panel of Figure 15 shows temperature fluctuations observed by Opportunity at $L_s = 142°$ and about 12:35 local time. This was a time of strong activity, with temperatures within 100 m of the surface varying by 5 K from peak to peak. The temperature fluctuations here represent the movement of warm and cool parcels of air through the Mini-TES field-of-view, and they appear to occur with both random amplitude and random duration. The individual temperature fluctuations observed here can last as long as one minute, or as short as 10 seconds. The amplitude of the fluctuations decreases dramatically above about 100 m. That is also the height of the top of the near-surface highly superadiabatic layer (see section 4.1 and Figure 10), which indicates that the turbulent motions observed here are associated with conditions within that near-surface layer.

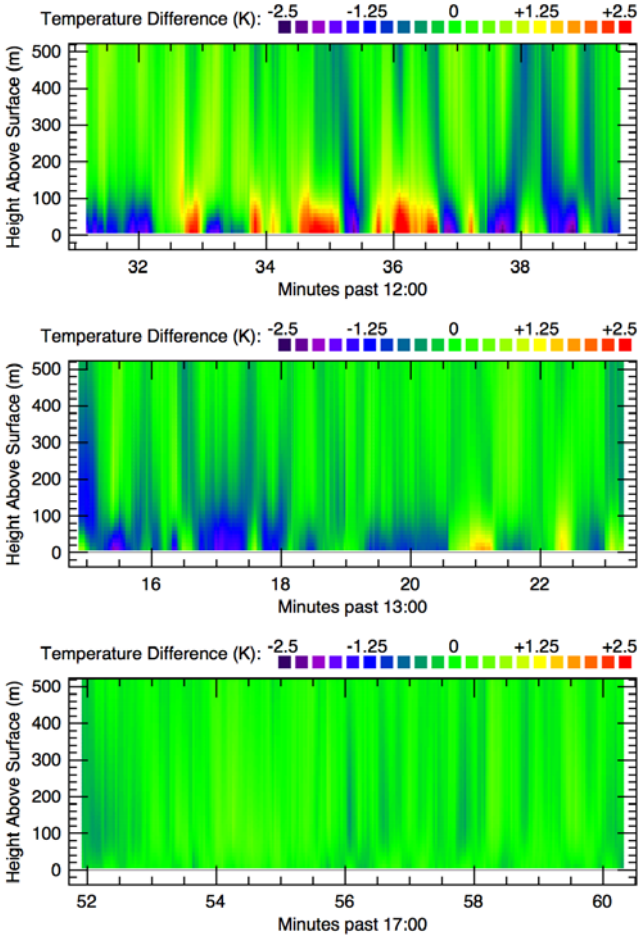

Figure 15. Near-surface temperature fluctuations observed by Opportunity. The temperature retrieval has been performed on each individual Mini-TES spectrum to give a profile every two seconds. At each height the time-averaged temperature has been subtracted to show the time-variable portion of the thermal field. The green color represents average temperature, while yellow and red represent warmer than average temperatures and blue and purple represent cooler than average temperatures. The color scale ranges from −2.5 K (purple) to +2.5 K (red). The top panel shows midday observations by Opportunity at $L_s = 142°$. The middle panel shows midday observations by Opportunity at $L_s = 145°$ (six days after the observations shown in the top panel). The bottom panel shows early evening observations by Opportunity at $L_s = 140°$ (three days prior to the observations shown in the top panel).

[60] The middle panel of Figure 15 shows conditions observed by Opportunity at nearly the same local time and just six days after that shown in the top panel. During the period shown in the middle panel there was significantly less turbulent activity, with only very occasional fluctuations of much lower amplitude. At a given local time, the amount of convective activity that causes the temperature fluctuations can vary significantly from day to day.

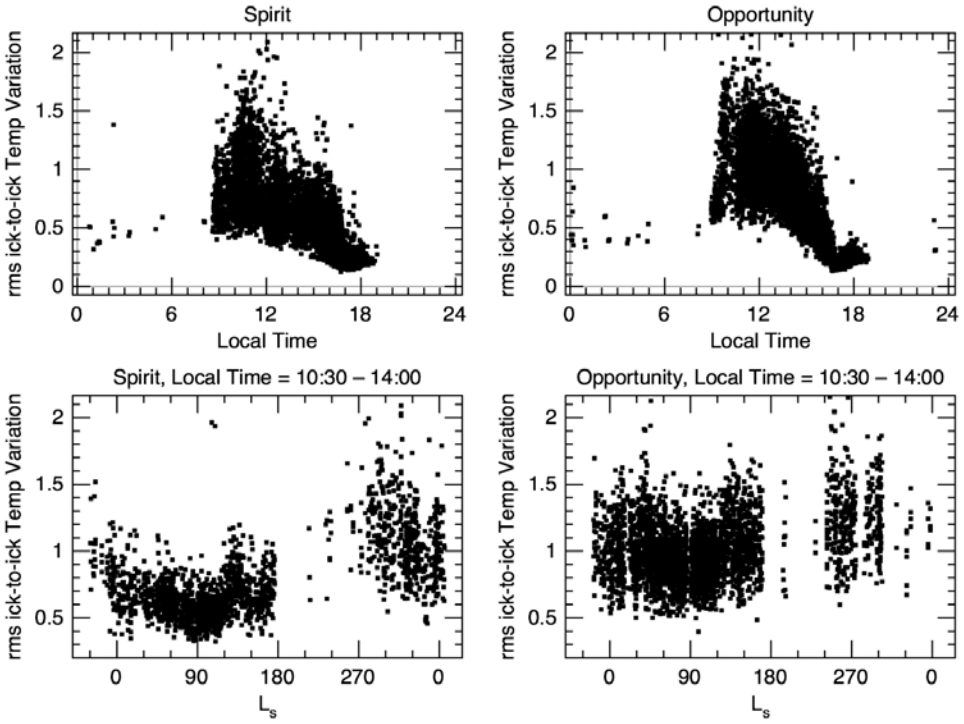

Figure 16. The root-mean-square (rms) spectrum-to-spectrum variation in the brightness temperature in the center of the CO_2 band (669 cm^{-1}). The signal at 669 cm^{-1} samples the lowest 50 m or so of the atmosphere where the temperature fluctuations have greatest amplitude. The rms temperature variation is a measure of the amount of convective activity present at the time. The top two panels show the dependence of the rms temperature variation on local time for all observations. The bottom two panels show the dependence on season (L_s) for midday observations.

[61] The bottom panel of Figure 15 shows observations from Opportunity at roughly the same season (L_s = 140°) during the evening. At this relatively late hour the near-surface superadiabatic layer has disappeared and along with it the turbulent motions that cause the temperature fluctuations. The remaining variations, which have amplitude of a couple tenths of a degree, are indicative of the level of noise in the retrievals.

[62] An easy way to estimate the amount of turbulent activity for a given Mini-TES observation is to evaluate the root-mean-square (rms) spectrum-to-spectrum variation in the brightness temperature in the center of the CO_2 band (669 cm^{-1}). Recalling Figure 5, the radiance at 669 cm^{-1} samples the lowest 50 m or so of the atmosphere where the temperature fluctuations have greatest amplitude. Figure 16 shows the rms spectrum-to-spectrum temperature variation as a function of local time and season as observed by both Spirit and Opportunity. The top two panels show a clear diurnal trend in the strength of the temperature fluctuations. Before 8:00 and after 17:00 local time, there is essentially no activity. The 0.5 K "background" level is indicative of the noise level. The strength of temperature fluctuations follows the diurnal trend of solar heating (and surface temperature) reaching a peak around 12:00. The day-to-day variability is also evident in the spread of points at a given local time.

[63] The bottom two panels of Figure 16 show the seasonal dependence of temperature fluctuations recorded during the active period between 10:30 and 14:00 local time. The seasonal trend of temperature fluctuations mirrors the seasonal trend of near-surface atmospheric temperatures (Figure 12) and surface temperature.

5. Discussion

5.1. Comparison Between Spirit and Opportunity

[64] The simultaneous operation of two rovers on opposite sides of the planet allows for a direct comparison of atmospheric conditions at the two sites (Spirit landed in Gusev Crater at 14.6°S, 184.5°W), while Opportunity landed on Meridani Planum at 1.9°S, 2.5°W). Overall, as shown in the previous section, the retrievals from Spirit and Opportunity observations share many of the same diurnal and seasonal trends. This is expected since both rovers landed at equatorial latitudes. However, there are some notable differences. Surface and atmospheric temperatures were generally warmer at Opportunity than at Spirit and there was a significant seasonal difference between the two. The top panel of Figure 17 shows late-afternoon temperatures 100 m above the surface observed by Spirit and Opportunity as a function of season. The amplitude of the observed seasonal variation was at least 10 K larger for Spirit than for Opportunity. While temperatures were similar during the perihelion season (L_s = 180° to 360°), temperatures remained noticeably warmer at Opportunity during the aphelion season (L_s = 0° to 180°). A similar pattern was observed at other heights and times of day. The annual mean temperature was about 5 K warmer at Opportunity, with a

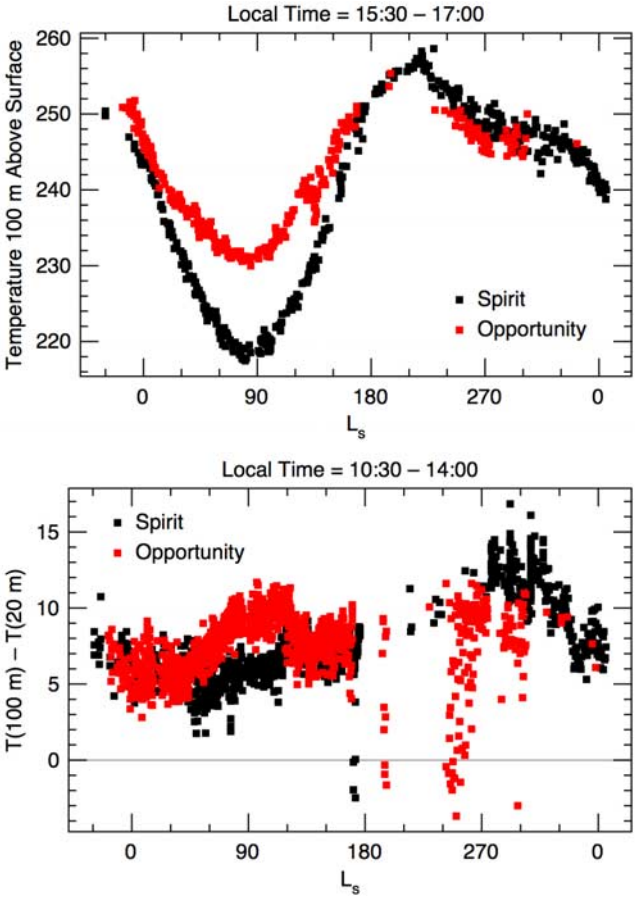

Figure 17. A comparison of temperatures observed by Spirit and Opportunity as a function of season (L_s). The top panel shows temperatures 100 m above the surface observed in the late afternoon (15:30–17:00 hours local time). The bottom panel shows the temperature difference (gradient) between 20 and 100 m above the surface for midday observations (10:30–14:00 hours local time).

maximum temperature difference about 12 K warmer near L_s = 90° and a minimum difference about 2 K cooler near L_s = 270°. The difference in seasonal variation is primarily caused by the latitude difference between the two sites, with Opportunity seeing a smaller seasonal effect because of its more equatorial location. The mean difference of 5 K is caused by the lower surface albedo at the Opportunity landing site [*Golombek et al.*, 2005; *Bell et al.*, 2004a, 2004b].

[65] The bottom panel of Figure 17 illustrates another difference between the two sites. Shown is the temperature difference between 20 and 100 m above the surface between 10:30 and 14:00 local time as a function of season. This is a measure of the strength of the near-surface superadiabatic layer. Although roughly similar, the temperature gradient is systematically higher for Opportunity near L_s = 90° and lower near L_s = 270°. This pattern is also repeated in the bottom panel of Figure 16 showing the rms amplitude of temperature fluctuations.

[66] Dust optical depth and water vapor column abundance also showed systematic differences between the two rovers (see Figures 13 and 14). Dust optical depth was generally higher at Opportunity, especially during the low-dust aphelion season before the dust storms began (L_s = 40° to 140°). As noted earlier, differences in the detailed record of dust optical depth allows local-scale dust storms to be distinguished from regional- or global-scale dust storms. Water vapor abundance was systematically higher at Spirit than at Opportunity except during the period L_s = 90° to 180° when more water vapor was observed at Opportunity. The two sites showed different seasonal trends, with the annual maximum water vapor abundance arriving about 50° of L_s later at Spirit.

5.2. Comparison With TES and THEMIS Observations

[67] The Thermal Emission Spectrometer (TES) on board the Mars Global Surveyor provided near-continuous atmospheric monitoring of surface temperature, atmospheric temperatures, aerosol optical depth, and water vapor abundance until 31 August 2004 (Mars Year 27, L_s = 81°) [*Christensen et al.*, 2001; *Smith*, 2004]. Retrieved atmospheric parameters from Mini-TES can be directly compared against retrievals from concurrent TES observations during the first eight months of the MER mission (until L_s = 81°), and indirectly compared against TES climatology averages [*Smith*, 2006] after that. The Thermal Emission Imaging System (THEMIS) on board the Mars Odyssey [*Christensen et al.*, 2004c] provides estimates of dust and ice optical depth (but not near-surface atmospheric temperature or water vapor abundance) [*Smith et al.*, 2003] throughout the period of time that Spirit and Opportunity have been in operation.

[68] Atmospheric temperature profiles retrieved from orbit using TES spectra cannot resolve the boundary layer structure revealed by Mini-TES, but overall seasonal trends can still be compared by looking at (for example) mid-afternoon Mini-TES temperatures 1000 m above the surface and the TES temperatures lowest to the surface. The TES and Mini-TES data show similar seasonal trends with minimum and maximum temperatures at the same seasons. The amplitude of the seasonal cycle is also similar (as much as can be compared with the two different data sets). In particular, the amplitude of the seasonal variation in atmospheric temperatures is larger at the Spirit site than at the Opportunity site in the TES observations, just as in the Mini-TES observations, although the difference in amplitude is somewhat smaller in the TES observations. This indicates that the difference in the amplitude of the seasonal variation in atmospheric temperatures between Spirit and Opportunity observed by Mini-TES may also have a component caused by local meteorology in addition to the latitude effect described earlier.

[69] Both TES and THEMIS observed the December 2003 dust storm that preceded the MER landings. The gradual clearing of that storm, and the clear aphelion season that followed that was observed by Mini-TES was also observed by TES and THEMIS. The reappearance of dust activity at L_s = 140° was unexpectedly early, but THEMIS observations do clearly show this early-season dust storm activity in a relatively narrow band centered on the equator between 20°N and 20°S latitude (covering both rover locations). THEMIS also shows significant low-latitude dust activity at L_s = 180°, 220°, and 310° [*Smith*, 2006],

which mirrors the trend of large storms seen at the two rover locations. One difference in the observations of dust optical depth is that the retrieved values from orbit tend to be systematically lower than those retrieved from Mini-TES by 10–50%. This difference might be explained by a combination of a vertical distribution of dust that is different than the well-mixed profile assumed here (and for TES retrievals), and the effect of directional surface emissivity on Mini-TES observations. A more detailed discussion of the comparison of dust optical depth between Mini-TES and TES is given by *Wolff et al.* [2006].

5.3. What About Water Ice Clouds?

[70] The algorithm described in section 3.2 is able to retrieve both dust and water ice, but in section 4 we have only shown results for dust optical depth. This is because the water ice optical depth retrieved from Mini-TES is either very small or consistent with zero. There are certainly some water ice clouds present at the rover sites, at least during the aphelion season. Orbital observations by TES [*Smith*, 2004] show a peak optical depth of 0.05–0.1 at both sites during L_s = 60° to 120°, and imaging from the rovers themselves shows thin, wispy water ice clouds.

[71] The lack of a definitive identification of water ice clouds in Mini-TES data leads to two conclusions. First, the water ice clouds may simply be less common at the rover sites than in the surrounding region [*Wolff et al.*, 2005], perhaps because of local-scale meteorology. And second, the clouds that do exist are relatively high (and not predominantly in ground fogs, for example). If water ice clouds are relatively high (with a base above 20 km), then they are both relatively cool, which gives a reduced signal, and also partially screened by dust, which obscures even further the ice cloud spectral features. This is discussed further by *Wolff et al.* [2006]. Ice clouds can still potentially be observed using Mini-TES, but the sensitivity to them is lower than from orbit.

5.4. Effect of Dust Storms on Near-Surface Temperatures

[72] The seasonal trend of atmospheric temperatures shows almost no effect of the large dust storms observed by Spirit near L_s = 140° and 220° (for example, compare Figures 12 and 13). On the other hand, effective surface temperatures retrieved from downward-looking Mini-TES observations were observed to drop by about 10 K in response to the dust storms. These observations are consistent with TES observations [*Smith et al.*, 2002, 2004], which show that while the heating effect of a dust storm can be tens of degrees above 20 km height, it is minimal in the lowest scale height.

6. Summary

[73] With more than a full Martian year of observations at two different locations on the surface of Mars, the Mini-TES instruments on board the Spirit and Opportunity rovers have provided a rich atmospheric data set that can be used to study the diurnal, seasonal, and even spatial dependence of column-integrated dust optical depth and water vapor abundance, and temperatures in the lowest 2 km of the atmosphere.

[74] Atmospheric observations from Mini-TES reveal a dynamic planetary boundary layer with large variations on seasonal, diurnal, and sub-minute timescales. At both rover locations, the annual cycle of temperatures showed a steady cooling from landing ($L_s \sim 340°$) to L_s = 85° followed by a relatively rapid increase to a broad annual maximum temperature at L_s = 215° and then a more gradual cooling. The amplitude of the annual temperature cycle at 100 m height was 40 K for Spirit, but only about 25 K for Opportunity. The diurnal cycle of temperatures is marked by the development of a highly superadiabatic layer within 100–200 m of the surface which persists from about 9:30 to 16:30 hours local time. At night a deep (at least 1 km) inversion layer develops. On timescales of 15–60 seconds, daytime temperatures fluctuate up to 5 K within the highly superadiabatic layer as convective turbulence moves parcels of warmer and cooler air through the Mini-TES field of view.

[75] Dust activity was also notable. The relatively clear aphelion period after the gradual clearing of a regional dust storm that occurred before landing ended abruptly with unusually early dust storms at L_s = 140°. Both local-scale and regional-scale storms continued throughout the perihelion season until L_s = 310°. Water vapor abundance showed clear annual variations with unexpectedly low abundance at the Opportunity site.

[76] The two Mini-TES instruments continue to operate and to extend the existing data set of atmospheric observations. Although calibration is increasingly challenging given the accumulation of dust on the instrument optics and secular drift in the instrument response function, new observations will provide important new information about interannual variation in the planetary boundary layer.

[77] **Acknowledgments.** We wish to thank all the scientists and engineers who made the MER mission possible. We especially thank the Mini-TES team for their help in obtaining the observations presented here. We acknowledge and thank John Wilson and Bob Haberle for making their model results available to us to estimate surface pressure, and we thank Dan Tyler and Claire Newman for their helpful referee reviews. This work was funded by NASA through the Mars Exploration Rover Project, a portion of which was carried out at the Jet Propulsion Laboratory, California Institute of Technology, under a contract with the National Aeronautics and Space Administration.

References

Bandfield, J. L., and M. D. Smith (2003), Multiple emission angle surface-atmosphere separations of Thermal Emission Spectrometer data, *Icarus*, *161*, 47–65.

Bell, J. F., III, et al. (2003), Mars Exploration Rover Athena Panoramic Camera (Pancam) investigation, *J. Geophys. Res.*, *108*(E12), 8063, doi:10.1029/2003JE002070.

Bell, J. F., III, et al. (2004a), Pancam multispectral imaging results from the Spirit rover at Gusev crater, *Science*, *305*, 800–806.

Bell, J. F., III, et al. (2004b), Pancam multispectral imaging results from the Opportunity rover at Meridiani Planum, *Science*, *306*, 1703–1709.

Christensen, P. R., et al. (2001), Mars Global Surveyor Thermal Emission Spectrometer experiment: Investigation description and surface science results, *J. Geophys. Res.*, *106*, 23,823–23,871.

Christensen, P. R., et al. (2003), Miniature Thermal Emission Spectrometer for the Mars Exploration Rovers, *J. Geophys. Res.*, *108*(E12), 8064, doi:10.1029/2003JE002117.

Christensen, P. R., et al. (2004a), Initial results from the Mini-TES experiment in Gusev Crater from the Spirit Rover, *Science*, *305*, 837–842.

Christensen, P. R., et al. (2004b), Mineralogy at Meridiani Planum from the Mini-TES experiment on the Opportunity Rover, *Science*, *306*, 1733–1739.

Christensen, P. R., et al. (2004c), The Thermal Emission Imaging System (THEMIS) for the Mars 2001 Odyssey mission, *Space Sci. Rev.*, *110*, 85–130.

Clancy, R. T., B. J. Sandor, M. J. Wolff, P. R. Christensen, M. D. Smith, J. C. Pearl, B. J. Conrath, and R. J. Wilson (2000), An intercomparison of ground-based millimeter, MGS TES, and Viking atmospheric temperature measurements: Seasonal and interannual variability of temperature and dust loading in the global Mars atmosphere, *J. Geophys. Res.*, *105*, 9553–9572.

Conrath, B. J. (1972), Vertical resolution of temperature profiles obtained from remote radiation measurements, *Icarus*, *29*, 1262–1271.

Conrath, B. J. (1975), Thermal structure of the Martian atmosphere during the dissipation of the dust storm of 1971, *Icarus*, *24*, 36–46.

Conrath, B. J., R. Curran, R. Hanel, V. Kunde, W. Maguire, J. Pearl, J. Pirraglia, and J. Welker (1973), Atmospheric and surface properties of Mars obtained by infrared spectroscopy on Mariner 9, *J. Geophys. Res.*, *78*, 4267–4278.

Conrath, B. J., P. J. Gierasch, M. D. Smith, and E. A. Ustinov (1994), Simultaneous retrieval of temperature and para hydrogen in Neptune's atmosphere, *Bull. Am. Astron. Soc.*, *26*, 1095.

Conrath, B. J., J. C. Pearl, M. D. Smith, W. C. Maguire, P. R. Christensen, S. Dason, and M. S. Kaelberer (2000), Mars Global Surveyor Thermal Emission Spectrometer (TES) observations: Atmospheric temperatures during aerobraking and science phasing, *J. Geophys. Res.*, *105*, 9509–9520.

Golombek, M. P., et al. (2005), Assessment of Mars Exploration Rover landing site predictions, *Nature*, *436*, 44–48.

Goody, R. M., and Y. L. Yung (1989), *Atmospheric Radiation: Theoretical Basis*, 2nd ed., Oxford Univ. Press, New York.

Goody, R., R. West, L. Chen, and D. Crisp (1989), The correlated-k method for radiation calculations in nonhomogenous atmospheres, *J. Quant. Spectrosc. Radiat. Transfer*, *42*, 539–550.

Grassi, D., N. I. Ignatiev, L. V. Zasova, A. Maturilli, V. Formissano, G. A. Bianchini, and M. Giuranna (2005), Methods for the analysis of data from the Planetary Fourier Spectrometer on the Mars Express Mission, *Planet. Space Sci.*, *53*, 1017–1034.

Hess, S. L., R. M. Henry, C. B. Leovy, J. A. Ryan, and J. E. Tillman (1977), Meteorological results from the surface of Mars: Viking 1 and 2, *J. Geophys. Res.*, *82*, 4559–4574.

Hinson, D. P., R. A. Simpson, J. D. Twicken, G. L. Tyler, and F. M. Flasar (1999), Initial results from radio occultation measurements with Mars Global Surveyor, *J. Geophys. Res.*, *104*, 26,997–27,012.

Hinson, D. P., M. D. Smith, and B. J. Conrath (2004), Comparison of atmospheric temperatures obtained through infrared sounding and radio occultation by Mars Global Surveyor, *J. Geophys. Res.*, *109*, E12002, doi:10.1029/2004JE002344.

Kliore, A. J., G. Fjeldbo, B. L. Siedel, M. J. Sykes, and P. M. Woiceshyn (1973), S band radio occultation measurements of the atmosphere and topography of Mars with Mariner 9: Extended mission coverage of polar and intermediate latitudes, *J. Geophys. Res.*, *78*, 4331–4351.

Jaquin, F., P. J. Gierasch, and R. Kahn (1986), The vertical structure of limb hazes in the Martian atmosphere, *Icarus*, *68*, 442–461.

Lacis, A. A., and V. Oinas (1991), A description of the correlated-k distribution method for modeling nongray gaseous absorption, thermal emission, and multiple scattering in vertically inhomogeneous atmospheres, *J. Geophys. Res.*, *96*, 9027–9063.

Landis, G. (2005), Exploring Mars with solar-powered rovers, in *Proceedings of the 31st IEEE Photovoltaic Specialists Conference*, pp. 858–861, Inst. of Electron. and Electr. Eng., New York.

Lemmon, M. T., et al. (2004), Atmospheric imaging results from the Mars Exploration Rovers: Spirit and Opportunity, *Science*, *306*, 1753–1756.

Lindal, G. F., H. B. Hotz, D. N. Sweetnam, Z. Shippony, J. P. Brenkle, G. V. Hartsell, and R. T. Spear (1979), Viking radio occultation measurements of the atmosphere and topography of Mars: Data acquired during 1 Martian year of tracking, *J. Geophys. Res.*, *84*, 8443–8456.

Michaels, T. I., and S. C. R. Rafkin (2004), Large-eddy simulation of atmospheric convection on Mars, *Q. J. R. Meteorol. Soc.*, *130*, 1251–1274.

Pollack, J. B., D. Colburn, R. Kahn, J. Hunter, W. Van Camp, C. E. Carlston, and M. R. Wolf (1977), Properties of aerosols in the Martian atmosphere as inferred from Viking lander imaging data, *J. Geophys. Res.*, *82*, 4479–4496.

Rothman, L. S., et al. (2005), The *HITRAN* 2004 molecular spectroscopic database, *J. Quant. Spectrosc. Radiat. Transfer*, *96*, 139–204.

Santee, M., and D. Crisp (1993), Thermal structure and dust loading on the Martian atmosphere during late southern summer: Mariner 9 revisited, *J. Geophys. Res.*, *98*, 3261–3279.

Savijärvi, H., A. Määttänen, J. Kauhanen, and A.-M. Harri (2004), Mars Pathfinder: New data and new model simulations, *Q. J. R. Meteorol. Soc.*, *130*, 669–683.

Schofield, J. T., J. R. Barnes, D. Crisp, R. M. Haberle, S. Larsen, J. A. Magalhães, J. R. Murphy, A. Seiff, and G. Wilson (1997), The Mars Pathfinder atmospheric structure investigation/meteorology (ASIMET) experiment, *Science*, *278*, 1752–1758.

Seiff, A., and D. B. Kirk (1977), Structure of the atmosphere of Mars in summer at mid-latitudes, *J. Geophys. Res.*, *82*, 4364–4378.

Smith, M. D. (2002), The annual cycle of water vapor on Mars as observed by the Thermal Emission Spectrometer, *J. Geophys. Res.*, *107*(E11), 5115, doi:10.1029/2001JE001522.

Smith, M. D. (2003), TES limb-geometry observations of aerosols, in *Proceedings of the 6th International Conference on Mars*, Abstract 3174, Lunar and Planet. Inst., Houston, Tex.

Smith, M. D. (2004), Interannual variability in TES atmospheric observations of Mars during 1999–2003, *Icarus*, *167*, 148–165.

Smith, M. D. (2006), TES atmospheric temperature, aerosol optical depth, and water vapor observations 1999–2004, paper presented at The Second Workshop on Mars Atmosphere Modelling and Observations, Cent. Natl. d'Etudes Spatiales, Granada, Spain.

Smith, M. D., B. J. Conrath, J. C. Pearl, and E. A. Ustinov (1996), Retrieval of atmospheric temperatures in the Martian planetary boundary layer using upward-looking infrared spectra, *Icarus*, *124*, 586–597.

Smith, M. D., J. C. Pearl, B. J. Conrath, and P. R. Christensen (2000), Mars Global Surveyor Thermal Emission Spectrometer (TES) observations of dust opacity during aerobraking and science phasing, *J. Geophys. Res.*, *105*, 9539–9552.

Smith, M. D., J. C. Pearl, B. J. Conrath, and P. R. Christensen (2002), Thermal Emission Spectrometer observations of Martian planet-encircling dust storm 2001a, *Icarus*, *157*, 259–263.

Smith, M. D., J. L. Bandfield, P. R. Christensen, and M. I. Richardson (2003), Thermal Emission Imaging System (THEMIS) infrared observations of atmospheric dust and water ice cloud optical depth, *J. Geophys. Res.*, *108*(E11), 5115, doi:10.1029/2003JE002115.

Smith, M. D., et al. (2004), First atmospheric science results from the Mars Exploration Rovers Mini-TES, *Science*, *306*, 1750–1753.

Smith, P. H., et al. (1997), Results from the Mars Pathfinder Camera, *Science*, *278*, 1758–1765.

Spanovich, N., M. D. Smith, P. H. Smith, M. J. Wolff, P. R. Christensen, and S. W. Squyres (2006), Surface and near-surface atmospheric temperatures from the Mars Exploration Rover landing sites, *Icarus*, *180*, 314–320.

Squyres, S. W., et al. (2004a), The Spirit Rover's Athena science investigation at Gusev Crater, Mars, *Science*, *305*, 794–799.

Squyres, S. W., et al. (2004b), The Opportunity Rover's Athena science investigation at Meridiani Planum, Mars, *Science*, *306*, 1698–1703.

Sutton, J. L., C. B. Leovy, and J. E. Tillman (1978), Diurnal variations of the Martian surface layer meteorological parameters during the first 45 sols at two Viking lander sites, *J. Atmos. Sci.*, *35*, 2346–2355.

Thomas, G. E., and K. Stamnes (1999), *Radiative Transfer in the Atmosphere and Ocean*, Cambridge Univ. Press, New York.

Wolff, M. J., and R. T. Clancy (2003), Constraints on the size of Martian aerosols from Thermal Emission Spectrometer observations, *J. Geophys. Res.*, *108*(E9), 5097, doi:10.1029/2003JE002057.

Wolff, M. J., R. T. Clancy, D. Banfield, and K. Cuozzo (2005), Water ice clouds as seen from the Mars Exploration Rovers, *Eos Trans. AGU*, *86*(52), Fall Meet. Suppl., Abstract P21E-02.

Wolff, M. J., et al. (2006), Constraints on dust aerosols from the Mars Exploration Rovers using MGS overflights and Mini-TES, *J. Geophys. Res.*, doi:10.1029/2006JE002786, in press.

D. Banfield and S. W. Squyres, Department of Astronomy, Cornell University, Ithaca, NY 14853, USA.

P. R. Christensen, Department of Geological Sciences, Arizona State University, Tempe, AZ 85287, USA.

A. Ghosh, Tharsis Inc., Gaithersburg, MD, USA.

G. A. Landis, NASA Glenn Research Center, Cleveland, OH 44135, USA.

M. D. Smith, NASA Goddard Space Flight Center, Code 693, Greenbelt, MD 20771, USA. (michael.d.smith@nasa.gov)

N. Spanovich, Jet Propulsion Laboratory, Pasadena, CA 91125, USA.

M. J. Wolff, Space Science Institute, Boulder, CO, USA.